Novel quality-effective zooming algorithm for color filter array

Kuo-Liang Chung
Wei-Jen Yang
National Taiwan University of Science and Technology
Department of Computer Science and Information Engineering
No. 43, Section 4, Keelung Road
Taipei, Taiwan 10672
E-mail: wjyang@mail.ntust.edu.tw

Jun-Hong Yu
National Taiwan University
Graduate Institute of Networking and Multimedia
No. 1, Section 4, Roosevelt Road
Taipei, Taiwan 10617

Wen-Ming Yan
National Taiwan University
Department of Computer Science and Information Engineering
No. 1, Section 4, Roosevelt Road
Taipei, Taiwan 10617

Chiou-Shann Fuh
National Taiwan University
Graduate Institute of Networking and Multimedia
and
Department of Computer Science and Information Engineering
No. 1, Section 4, Roosevelt Road
Taipei, Taiwan 10617

Abstract. *Mosaic images are captured by a single charge-coupled device/complementary metal-oxide-semiconductor (CCD/CMOS) sensor with the Bayer color filter array. We present a new quality-effective zooming algorithm for mosaic images. First, based on adaptive heterogeneity projection masks and Sobel- and luminance-estimation-based masks, more accurate gradient information is extracted from the mosaic image directly. According to the extracted gradient information, the mosaic green (G) channel is first zoomed. To reduce color artifacts, instead of directly moving the original red (R) value to its right position and the blue (B) value to its lower position, the color difference interpolation is utilized to expand the G-R and G-B color difference values. Finally, the zoomed mosaic R and B channels can be constructed using the zoomed G channel and the two expanded color difference values; afterward, the zoomed mosaic image is obtained. Based on 24 popular test mosaic images, experimental results demonstrate that the proposed zooming algorithm has more than* 1.79 dB *quality improvement when compared with two previous zooming algorithms, one by Battiato et al. (2002) and the other by Lukac et al. (2005).* © *2010 SPIE and IS&T.* [DOI: 10.1117/1.3302126]

1 Introduction

To reduce the manufacturing cost of digital cameras, instead of using three CCD/CMOS sensors, most manufacturers use a single sensor array to capture the color information based on the Bayer color filter array (CFA) structure,[1] which is depicted in Fig. 1. As a result, each pixel in the mosaic image has only one color component. Because the *G* channel is the most important factor to determine the luminance of the color image, half of the pixels in the Bayer CFA structure are assigned to the *G* channel; the *R* and *B* channels share the remaining parts evenly.

Since the full-color image is required for the human visual system, the two missing color components for each pixel in the mosaic image should be recovered as best as possible and such a recovery is called the demosaicing

Paper 09016RR received Feb. 6, 2009; revised manuscript received Nov. 18, 2009; accepted for publication Dec. 11, 2009; published online Feb. 23, 2010.

1017-9909/2010/19(1)/013005/15/$25.00 © 2010 SPIE and IS&T.

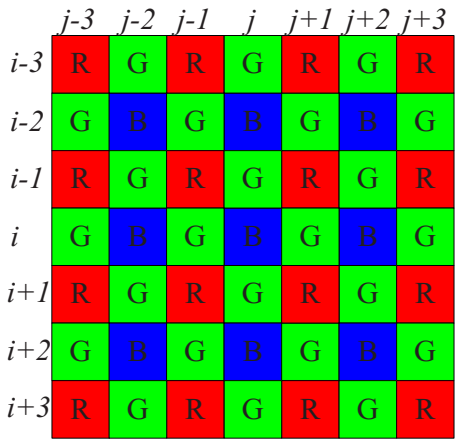

Fig. 1 Bayer CFA structure.

process.[2,3] Previously published demosaicing algorithms could be divided into two categories,[4] namely, the nonheuristic demosaicing algorithms and the heuristic demosaicing algorithms. In the first category, these developed nonheuristic demosaicing algorithms include the minimum mean squared error estimator method,[5] the projection-onto-convex-set method,[6] the linear hyper-plane method,[7] the Fourier domain-based methods,[8–10] the wavelet domain method,[11] and the Taylor expansion method.[12] The second category includes the bilinear interpolation method,[13] which is the simplest demosaicing method in which two missing color components of each pixel are calculated by averaging its proper adjacent pixels; the edge-sensing-based methods,[14–21] which can preserve the detailed edge information or limit the hue transitions; the color-difference-based hybrid methods[4,22–29] in which these methods were developed by integrating the interpolation estimation, edge-sensing scheme, and the color difference technique.

Besides the demosaicing issue, designing efficient zooming algorithms for mosaic images has received growing attention. Because the optical hardware zooming approach costs too much, the software zooming approach is preferable. For gray images or full-color images, some efficient zooming algorithms[30–32] have been developed. However, these developed algorithms can not be applied to zoom mosaic images directly. Intuitively, the given mosaic image can be demosaiced first, and then one of these developed zooming algorithms is applied to the demosaiced full-color image; unfortunately, this intuitive approach must store an extra full-color image to be used in the later zooming process, so it is impractical due to the limited memory constraint of digital cameras.

Previously, several zooming algorithms for mosaic images were developed. All of them only use one array memory with the same size of the zoomed image. Based on the local adaptive zooming concept, Battiato *et al.*[33] presented the first zooming algorithm. Based on the adaptive edge-sensing mechanism, Lukac and Plataniotis[34] Lukac *et al.*[35] presented two better zooming algorithms to improve the zoomed image quality. Further, Lukac and Plataniotis[36] presented a computation-saving interpolation method to meet the real-time surveillance requirement. Note that the previous zooming algorithms mentioned here enlarge the original mosaic image with size $X \times Y$ to the one with size $2X \times 2Y$. In this paper, we follow the same size constraint. Developing a zooming algorithm to enlarge the mosaic image to the one with arbitrary size is still a challenging problem.

Table 1 Three possible heterogeneity projection masks

N	$M_{\mathrm{hp}}(N)$
5	[1 −2 0 2 −1]
7	[1 −4 5 0 −5 4 −1]
9	[1 −6 14 −14 0 14 −14 6 −1]

In this paper, a new quality-effective zooming algorithm for mosaic images is presented. Utilizing the adaptive heterogeneity projection masks and the Sobel- and luminance-estimation-based (SL-based) masks,[29] more accurate gradient information can be extracted from the input mosaic image directly. Then, based on the color difference concept and the extracted gradient information, the proposed quality-effective mosaic image zooming algorithm is presented. Based on 24 test mosaic images, the proposed zooming algorithm has more than 1.79 dB of quality improvement when compared with two previous zooming algorithms, one by Battiato *et al.*[33] and the other by Lukac *et al.*[35]

The remainder of this paper is organized as follows. Section 2 presents the adaptive heterogeneity projection masks and the SL-based masks used to extract gradient information from the mosaic image. In Sec. 3, combining the extracted gradient information and the color difference concept, the proposed quality-effective zooming algorithm for mosaic images is presented. Section 4 demonstrates some experimental results to show the quality advantage of the proposed zooming algorithm. Finally, some concluding remarks are addressed in Sec. 5.

2 Extracting Gradient Information from Mosaic Images

In this section, we describe the adaptive heterogeneity projection masks and the SL-based masks,[29] which are used to extract gradient information from the mosaic image directly. As shown in Fig. 1, the R, G, and B color pixels located at position (i,j) in the input mosaic image are denoted by $I^r_{\mathrm{mo}}(i,j)$, $I^g_{\mathrm{mo}}(i,j)$, and $I^b_{\mathrm{mo}}(i,j)$, respectively.

Based on the concept of adaptive heterogeneity projection,[29] Table 1 shows three possible heterogeneity projection masks with different sizes adopted in this paper. In Table 1, the terms N and $M_{\mathrm{hp}}(N)$ denote the mask size and the corresponding heterogeneity projection mask, respectively. Given a mosaic image I_{mo}, the horizontal heterogeneity projection map $\mathrm{HP}_{H\text{-map}}$ and the vertical heterogeneity projection map $\mathrm{HP}_{V\text{-map}}$ can be obtained by

$$\mathrm{HP}_{H-\mathrm{map}} = |I_{\mathrm{mo}} \otimes M_{\mathrm{hp}}(N)^T|,$$

-1	-2		2	1
-4	-8		8	4
-6	-12		12	6
-4	-8		8	4
-1	-2		2	1

-1	-4	-6	-4	-1
-2	-8	-12	-8	-2
2	8	12	8	2
1	4	6	4	1

Fig. 2 Two normalized SL-based masks: (a) the horizontal and (b) the vertical SL-based mask.

$$\mathrm{HP}_{V\text{-map}} = |I_{\mathrm{mo}} \otimes M_{\mathrm{hp}}(N)^T|, \tag{1}$$

where the symbol $\otimes$ denotes the 1-D convolution operator, $|\cdot|$ denotes the absolute value operator, and the operator T denotes the transpose operator. According to the statistical analysis, $N=5$ is a good choice to gather accurate horizontal and vertical edge information of the current pixel; it can also reduce the computation time for calculating Eq. (1). For exposition, the determined $N(=5)$ is called N_H.

To normalize the masks with different sizes, the normalization factor $1/Q_{N_H}$ is used to normalize the coefficients of the mask where the value of Q_{N_H} is defined as the sum of positive coefficients covered by the mask with size N_H. As a result, the heterogeneity projection mask $[1\ -2\ 0\ 2\ -1]^T$ would be normalized to $[1\ -2\ 0\ 2\ -1]^T/3$. To reduce the estimation error, we use the low-pass filter to tune the heterogeneity projection maps. For $\mathrm{HP}_{H\text{-map}}$ and $\mathrm{HP}_{V\text{-map}}$ the horizontal and vertical heterogeneity projection values at position (i,j) are denoted by $\mathrm{HP}_H(i,j)$ and $\mathrm{HP}_V(i,j)$, respectively. The tuned $\mathrm{HP}_H(i,j)$ and $\mathrm{HP}_V(i,j)$ can be computed by using the following two low-pass filters: $\mathrm{HP}'_H(i,j)=(1/10)\Sigma_{k=-4}^{4}\delta_k \mathrm{HP}_H(i,j+k)$ and $\mathrm{HP}'_V(i,j)=(1/10)\Sigma_{k=-4}^{4}\delta_k \mathrm{HP}_V(i+k,j)$, respectively, where $\delta_k=2$ if $k=0$; $\delta_k=1$, otherwise. The two tuned heterogeneity projection values of the current pixel at position (i,j) are used to determine the interpolation direction of the current pixel.

To extract gradient information from the mosaic image, we further embed the luminance estimation technique[8] into the Sobel operator;[37] the two normalized SL-based masks[29] are shown in Fig. 2. After running two SL-based masks on the 5×5 mosaic subimage centered at position (i,j), the horizontal gradient response $\Delta I^H_{\mathrm{dm}}(i,j)$ and the vertical gradient response $\Delta I^V_{\mathrm{dm}}(i,j)$ can be obtained. The obtained gradient responses are used to determine the interpolation weights for the neighboring pixels of the current pixel. In addition, from the hardware viewpoint in camera design, performing one multiplication requires more computational load and greater power consumption than that required using shift operation. We thus want to decrease the number of used multiplications when running the SL-based masks on the mosaic subimage. After examining two SL-based masks as shown in Fig. 2, we observe that only five numbers, 2, 4, 6, 8, and 12, are considered. Based on this observation, it requires only two multiplications, three shift operations, 19 additions, and 10 absolute-value operations rather than 20 multiplications, 19 additions, and 10 absolute-value operations to obtain one response by running the mask on the 5×5 mosaic subimage.

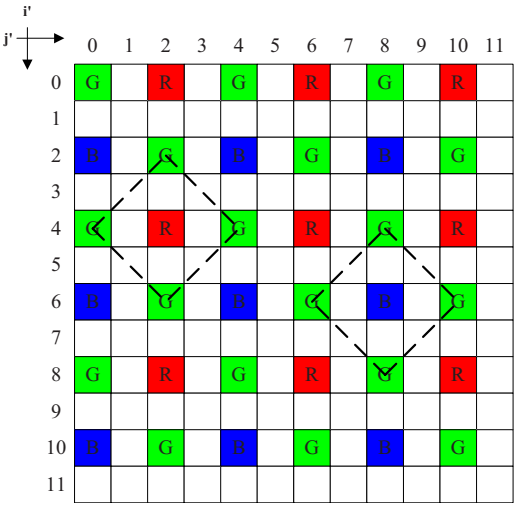

Fig. 3 Pattern of the obtained Z_{mo} after expanding I_{mo}.

3 Proposed Zooming Algorithm for Mosaic Images

The proposed quality-effective zooming algorithm consists of two stages: (1) zooming the mosaic G channel I^g_{mo} with size $X\times Y$ to obtain the zoomed mosaic G channel Z^g_{mo} with size $2X\times2Y$; (2) zooming the mosaic R channel I^r_{mo} and mosaic B channel I^b_{mo} to obtain the zoomed mosaic R channel Z^r_{mo} and zoomed mosaic B channel Z^b_{mo}. Finally, the zoomed mosaic image Z_{mo} can be obtained.

3.1 *Stage 1: Zooming the Mosaic G Channel*

Initially, the original mosaic image is expanded by the following rule:

$$Z_{\mathrm{mo}}(2i,2j) = I_{\mathrm{mo}}(i,j),$$

$$Z\mathrm{HP}'_d(2i,2j) = \mathrm{HP}'_d(i,j),$$

$$\Delta Z^d_{\mathrm{dm}}(2i,2j) = \Delta I^d_{\mathrm{mo}}(i,j), \tag{2}$$

where for all $d\in\{H,V\}$, $i\in\{0,1,2,\ldots,X-1\}$, and $j\in\{0,1,2,\ldots,Y-1\}$; $Z\mathrm{HP}'_d(i',j')$ and $\Delta Z^d_{\mathrm{dm}}(i',j')$ denote the tuned adaptive heterogeneity projection value and the gradient response at position (i',j') in the zoomed mosaic image Z_{mo}, respectively. After expanding I_{mo}, Fig. 3 illustrates the pattern of the obtained Z_{mo}. The zooming process for the mosaic G channel consists of two steps: (1) estimating the G values of the pixels in $\Omega^g_1=\{(4m,4n+2),(4m'+2,4n')\,|\,\forall m,m',n,n'\in\mathbb{Z},0\leq4m,4m'+2\leq2X-1,0\leq4n+2,4n'\leq2Y-1\}$; (2) estimating the G values of the pixels in $\Omega^g_2=\{(m,n)\,|\,\forall m,n\in\mathrm{odd},0\leq m\leq2X-1,0\leq n\leq2Y-1\}$. For exposition, the pixels in Ω^g_1 and Ω^g_2 are denoted by symbols ○ and ▲ in Fig. 4, respectively. The detailed descriptions for the two steps are demonstrated in Secs. 3.1.1 and 3.1.2, respectively.

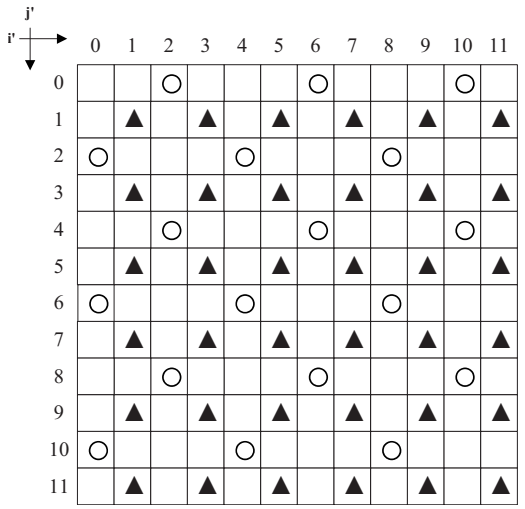

Fig. 4 Depiction of the pixels in Ω_1^g and Ω_2^g, where $\bigcirc \in \Omega_1^g$ and $\blacktriangle \in \Omega_2^g$.

3.1.1 *Step 1 in stage 1: estimating the G values of the pixels in* Ω_1^g

From Fig. 3, it is observed that for each pixel at position $(x,y) \in \Omega_1^g$, the G value can be estimated from its four neighboring G pixels with movement $\Omega_{n1}^g = \{(x',y') | (x',y') = (x \pm 2, y), (x, y \pm 2)\}$. Figure 5 is the representative to explain how to estimate the G value $Z_{\mathrm{mo}}^g(x,y)$. Considering the neighboring G pixel located at location $(x-2,y)$, if the vertical G gradient response $\Delta Z_{\mathrm{dm}}^V(x-2,y)$ is large, it means that there is a horizontal edge passing through it. Based on the color difference concept,[22,23] this case reveals that the G value of this pixel makes less contribution to the estimation of the G value for pixel $Z_{\mathrm{mo}}^g(x,y)$; otherwise, the G value of this pixel makes more contribution to the estimation of the G value for pixel $Z_{\mathrm{mo}}^g(x,y)$. Further, to reduce the estimation error, the two vertical G gradient responses $\Delta Z_{\mathrm{dm}}^V(x,y)$ and $\Delta Z_{\mathrm{dm}}^V(x-4,y)$ are also considered. Combining the preceding analysis, the weight of the pixel at location $(x-2,y)$ can be given by $w_g(V,x-2,y) = 1/\{1+[\Delta Z_{\mathrm{dm}}^V(x,y) + 2\Delta Z_{\mathrm{dm}}^V(x-2,y) + \Delta Z_{\mathrm{dm}}^V(x-4,y)]\}$. Following the similar discussion, the weights of the four neighboring G pixels can be expressed by $w_g(V,x-2,y) = 1/\{1+[\Sigma_{k=0}^2 \delta_k \Delta Z_{\mathrm{dm}}^V(x-2k,y)]\}$, $w_g(V,x+2,y) = 1/\{1+[\Sigma_{k=0}^2 \delta_k \Delta Z_{\mathrm{dm}}^V(x+2k,y)]\}$, $w_g(H,x,y-2) = 1/\{1+[\Sigma_{k=0}^2 \delta_k \Delta Z_{\mathrm{dm}}^H(x,y-2k)]\}$, and $w_g(H,x,y+2) = 1/\{1+[\Sigma_{k=0}^2 \delta_k \Delta Z_{\mathrm{dm}}^H(x,y+2k)]\}$, where $\delta_k = 2$ if $k=1$; $\delta_k = 1$, otherwise.

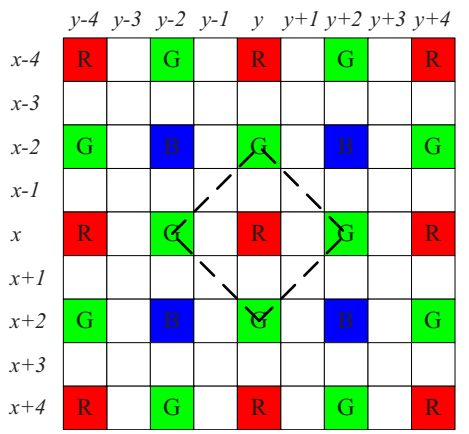

Fig. 5 Subimage used to explain how to estimate the G values of pixels in Ω_1^g.

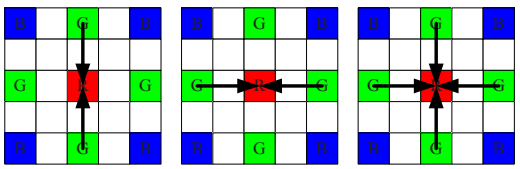

Fig. 6 Data dependence of the proposed interpolation estimation for the G channel: (a) horizontal variation (vertical edge), (b) vertical variation (horizontal edge), and (c) other variations.

In addition, based on the horizontal and vertical heterogeneity projection values of the current pixel at position (x,y), $ZHP'_H(x,y)$ and $ZHP'_V(x,y)$, the interpolation estimation scheme for G channel should consider three cases, namely (1) horizontal variation as shown in Fig. 6(a), (2) vertical variation as shown in Fig. 6(b), and (3) the other variations as shown in Fig. 6(c). The arrows in Fig. 6 denote the relevant data dependence. Consequently, the value of $Z_{\mathrm{mo}}^g(x,y)$ can be estimated by

$$Z_{\mathrm{mo}}^g(x,y) = Z_{\mathrm{mo}}^r(x,y) + \frac{\sum_{(d,x',y') \in \xi_g} w_g(d,x',y') D_g(x',y')}{\sum_{(d,x',y') \in \xi_g} w_g(d,x',y')},$$

$$\xi_g = \begin{cases} \xi_1 & \text{if } ZHP'_V(x,y) < \alpha ZHP'_H(x,y) \\ \xi_2 & \text{if } ZHP'_H(x,y) < \alpha ZHP'_V(x,y) \\ \xi_1 \cup \xi_2 & \text{otherwise,} \end{cases} \quad (3)$$

where $\xi_1 = \{(V,x \pm 2,y)\}$ and $\xi_2 = \{(H,x,y \pm 2)\}$; if $(d,x',y') \in \xi_1$, $D_g(x',y') = Z_{\mathrm{mo}}^g(x',y') - [Z_{\mathrm{mo}}^r(x'+2,y') + Z_{\mathrm{mo}}^r(x'-2,y')]/2$, if $(d,x',y') \in \xi_2$, $D_g(x',y') = Z_{\mathrm{mo}}^g(x',y') - [Z_{\mathrm{mo}}^r(x',y'+2) + Z_{\mathrm{mo}}^r(x',y'-2)]/2$. Then, the proposed new refinement method, which combines the concept of the local color ratios[38] and the proposed weighting scheme, is used to refine the estimated $Z_{\mathrm{mo}}^g(x,y)$ by

$$Z_{\mathrm{mo}}^g(x,y) = -\beta + [Z_{\mathrm{mo}}^r(x,y) + \beta] \frac{\sum_{(d,x',y') \in \xi'_g} \delta_{(d,x',y')} w_g(d,x',y') L_g(x',y')}{\sum_{(d,x',y') \in \xi'_g} \delta_{(d,x',y')} w_g(d,x',y')}, \quad (4)$$

where $\xi'_g = \{(H,x,y),(V,x,y),(H,x,y \pm 2),(V,x \pm 2,y)\}$; $L_g(x',y') = [Z_{\mathrm{mo}}^g(x',y') + \beta]/[Z_{\mathrm{mo}}^r(x',y') + \beta]$; $\delta_{(d,x',y')} = (1/2)$ if $(d,x',y') \in \{(H,x,y),(V,x,y)\}$; $\delta_{(d,x',y')} = 1$, otherwise. Furthermore, the determination of the two parameters α and β is discussed in the appendix.

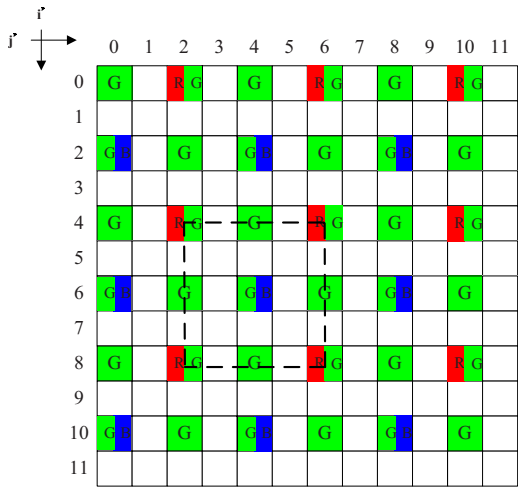

Fig. 7 Pattern of Z_{mo} after performing the estimation for the G values of pixels in Ω_1^g.

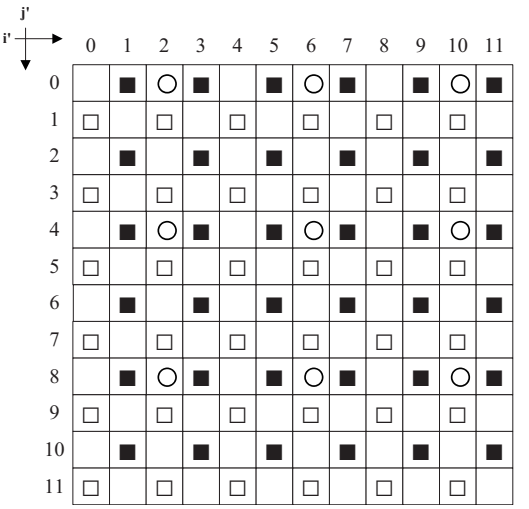

Fig. 9 Depiction of the pixels in Ω^r, Ω^{D_r}, and Ω^b, where ■ $\in \Omega^r$, ○ $\in \Omega^{D_r}$, and □ $\in \Omega^b$.

After estimating the G values in Ω_1^g, Fig. 7 illustrates the current pattern of Z_{mo}. For the current pattern of Z_{mo}, in order to preserve the Bayer CFA structure, Lukac and Plataniotis,[34] and Lukac *et al.*[35] suggested moving the R and B values of the pixels in Ω_1^g to the positions corresponding to the Bayer CFA structure. Thus, for each R value at position $(x',y') \in \Omega_1^g$, we move it to the right position $(x',y'+1)$; for each B value at position $(x',y') \in \Omega_1^g$, we move it to the lower position $(x'+1,y')$. After moving R and B values, the resultant pattern of Z_{mo} is illustrated in Fig. 8, and then the missing R and B color values can be estimated by the existent R and B color pixels. Unfortunately, moving the R value to its right position and the B value to its lower position directly would lead producing acute color artifacts in the nonhomogenous regions and degrading the image quality of the zoomed image.

To overcome this problem, instead of using the preceding approach, we use the color difference interpolation to expand the G-R color difference and the G-B color difference. Based on the Bayer CFA structure, it is known that the R pixels will be fully populated in $\Omega^r=\{(2m,2n+1)|m,n\in\mathbb{Z},0\leqslant 2m\leqslant 2X-1,0\leqslant 2n+1\leqslant 2Y-1\}$ after the zooming process. Further, for the pixels in $\Omega^{D_r}=\{(4m,4n+2)|m,n\in\mathbb{Z},0\leqslant 4m\leqslant 2X-1,0\leqslant 4n+2\leqslant 2Y-1\}$, the G-R color difference values can be calculated by $D_r(x',y')=Z_{mo}^g(x',y')-Z_{mo}^r(x',y'),\forall(x',y')\in\Omega^{D_r}$. For exposition, the pixels in Ω^r and Ω^{D_r} are denoted by the symbols ■ and ○, respectively, in Fig. 9. Then, we can estimate the color difference values of the pixels in Ω^r from the color difference values of the pixels in Ω^{D_r} by using the bilinear interpolation estimation. In Fig. 10, we observe that the G-R color difference values of the four corner pixels have been known. Using the bilinear interpolation estimation, the color difference values of the pixels at positions $\{(x+k_1,y+k_2)|k_1\in\{0,\pm 2\},k_2\in\{\pm 1\}\}$, which are denoted by gray colors, could be estimated by

$$D_r(x+k_1,y+k_2)=\sum_{\delta_1}\frac{2+\delta_1 k_2}{4}\sum_{\delta_2}\frac{2+\delta_2 k_1}{4}D_r(x+2\delta_2,y+2\delta_1), \quad (5)$$

where $\delta_1,\delta_2\in\{\pm 1\}$; $k_1\in\{0,\pm 2\}$; and $k_2\in\{\pm 1\}$. By the

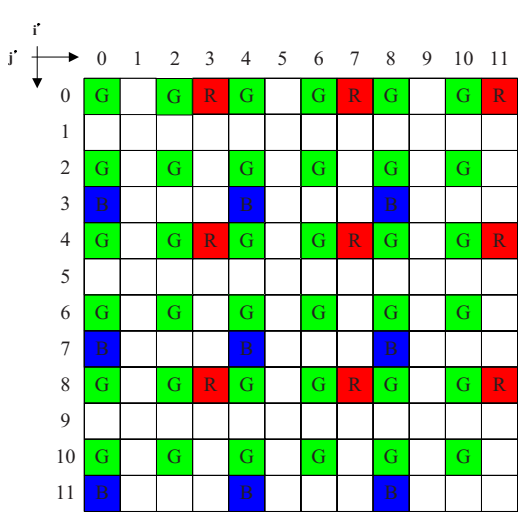

Fig. 8 Pattern of Z_{mo} after moving R and B values to the positions corresponding to the Bayer CFA structure.

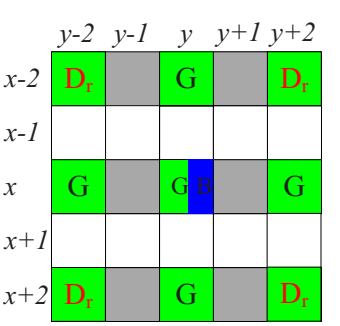

Fig. 10 Subimage used to explain how to estimate the color difference values of the pixels in Ω^r.

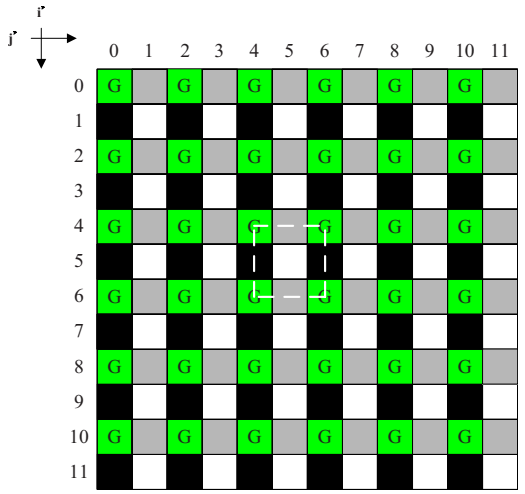

Fig. 11 Current pattern of Z_{mo} after estimating the color difference values of the pixels in Ω^r and Ω^b.

same arguments, the G-B color difference values of the pixels in $\Omega^b=\{(2m+1,2n)\,|\,m,n\in\mathbb{Z},0\leqslant 2m+1\leqslant 2X-1,0\leqslant 2n\leqslant 2Y-1\}$, i.e., the pixels denoted by □ in Fig. 9, can be estimated. Then, Fig. 11 illustrates the current pattern of Z_{mo} after estimating the G-B color difference values of the pixels in Ω^r and Ω^b. In Fig. 11, the pixels in Ω^r and Ω^b are denoted by gray colors and black colors, respectively.

3.1.2 *Step 2 in stage 1: estimating the G values of the pixels in Ω_2^g*

After describing how to estimate the G values of the pixels in Ω_1^g, we now describe how to estimate the G values of the pixels in Ω_2^g. After comparing the arrangement of the G channel in Fig. 12 with that of the R (or B) channel in the mosaic image (see Fig. 1), it is not hard to find that the arrangements of two channels are the same except the number of pixels in the two channels. From Ref. 29, we have known that the four SI-quad-masks, which are derived by combining the Sobel operator and the bilinear interpolation, can be used to extract the horizontal, vertical, $\pi/4$-diagonal, and $-\pi/4$-diagonal gradient information of

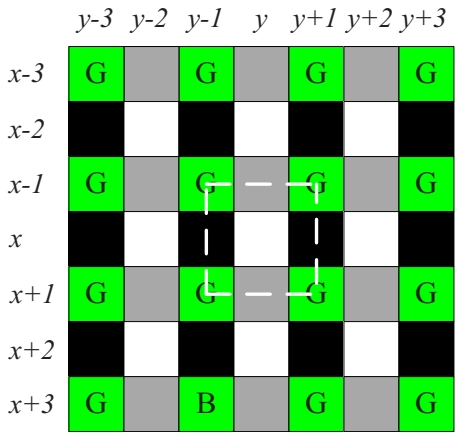

Fig. 12 Subimage used to explain how to estimate the G values of pixels in Ω_2^g.

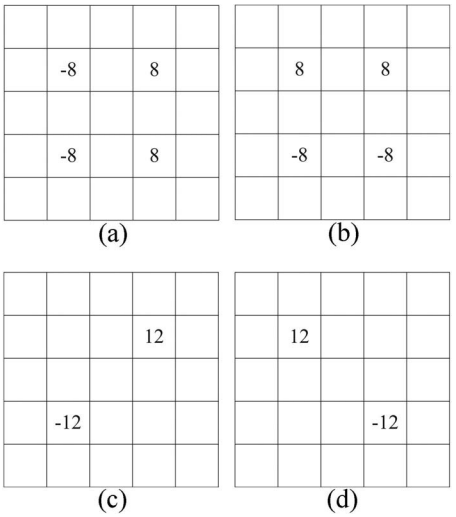

Fig. 13 For all pixels at positions $(x',y')\in\{(x\pm 2m,y\pm 2n)\}$ in Fig. 12, the four SI-based masks for G channel. (a) The horizontal SI-based mask. (b) The vertical SI-based mask. (c) The $\pi/4$-diagonal SI-based mask. (d) The $-\pi/4$-diagonal SI-based mask.

the R (or B) channel in the mosaic image as shown in Fig. 1. The four SI-quad-masks are shown in Figs. 13–16. Because the arrangement of the G channel in Fig. 12 is similar to that of the R (or B) channel in Fig. 1, we can directly use the four SI-quad-masks as shown in Figs. 13–16 to extract the G gradient information of all pixels in Z_{mo}.

From Fig. 12, it is observed that for each pixel at position $(x,y)\in\Omega_2^g$, the G value can be estimated from its four neighbors with movement $\Omega_{n_2}^g=\{(x',y')\,|\,(x',y')=(x\pm 1,y\pm 1)\}$. Similar to the G value estimation for pixels in Ω_1^g, to estimate $Z_{mo}^g(x,y)$ in Fig. 12 more accurately, four diagonal gradients are considered to determine the four proper weights.

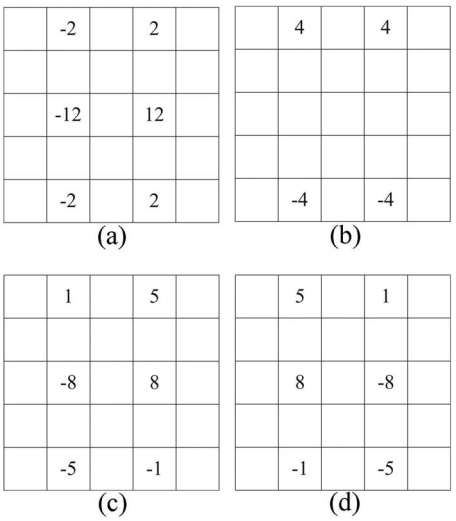

Fig. 14 For all pixels at positions $(x',y')\in\{(x\pm 2m+1,y\pm 2n)\}$ in Fig. 12, the four SI-based masks for G channel. (a) The horizontal SI-based mask. (b) The vertical SI-based mask. (c) The $\pi/4$-diagonal SI-based mask. (d) The $-\pi/4$-diagonal SI-based mask.

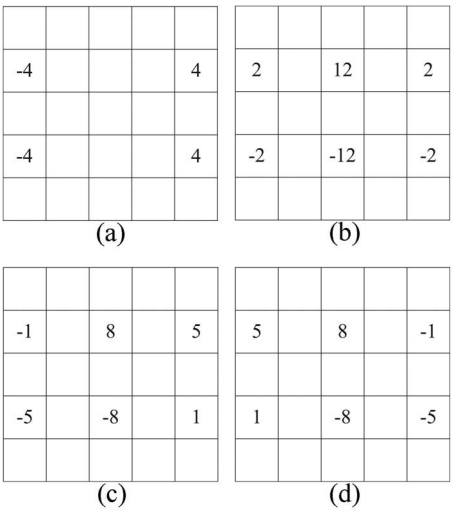

Fig. 15 For all pixels at positions $(x',y') \in \{(x\pm 2m, y\pm 2n+1)\}$ in Fig. 12, the four SI-based masks for G channel (a) The horizontal SI-based mask. (b) The vertical SI-based mask. (c) The $\pi/4$-diagonal SI-based mask. (d) The $-\pi/4$-diagonal SI-based mask.

Considering the neighboring G pixel located at location $(x-1,y-1)$, if there is a $\pi/4$-diagonal edge passing through it, i.e., the $-\pi/4$-diagonal G gradient response $\Delta Z_{\mathrm{dm}}^{-\pi/4,g}(x-1,y-1)$ is large, the G value of this pixel makes less contribution to the estimation of $Z_{\mathrm{mo}}^{g}(x,y)$, otherwise, the G value of this pixel makes more contribution to the estimation of $Z_{\mathrm{mo}}^{g}(x,y)$. Further, to reduce the estimation error, the two $-\pi/4$-diagonal G gradient responses $\Delta Z_{\mathrm{dm}}^{-\pi/4,g}(x,y)$ and $\Delta Z_{\mathrm{dm}}^{-\pi/4,g}(x-2,y-2)$ are also considered. Consequently, the weight of the pixel at location $(x-1,y-1)$ can be given by $w_g(V,x-1,y-1)=1/\{1+[\Delta Z_{\mathrm{dm}}^{-\pi/4,g}(x,y)+2\Delta Z_{\mathrm{dm}}^{-\pi/4,g}(x-1,y-1)+\Delta Z_{\mathrm{dm}}^{-\pi/4,g}(x-2,y-2)]\}$. Similarly, the weights of the four neighboring G pixels can be expressed by $w_g(-\pi/4,x-1,y-1)=1/\{1+[\sum_{k=0}^{2}\delta_k\Delta Z_{\mathrm{dm}}^{-\pi/4,g}(x-k,y-k)]\}$, $w_g(\pi/4,x-1,y+1)=1/\{1+[\sum_{k=0}^{2}\delta_k\Delta Z_{\mathrm{dm}}^{\pi/4,g}(x-k,y+k)]\}$, $w_g(\pi/4,x+1,y-1)=1/\{1+[\sum_{k=0}^{2}\delta_k\Delta Z_{\mathrm{dm}}^{\pi/4,g}(x+k,y-k)]\}$, and $w_g(-\pi/4,x+1,y+1)=1/\{1+[\sum_{k=0}^{2}\delta_k\Delta Z_{\mathrm{dm}}^{-\pi/4,g}(x+k,y+k)]\}$, where $\delta_k=2$ if $k=1$; $\delta_k=1$, otherwise. According to the preceding description, the G value of $Z_{\mathrm{mo}}^{g}(x,y)$ in Fig. 12 can be estimated by

$$Z_{\mathrm{mo}}^{g}(x,y)=\frac{\sum_{(d,x',y')\in\xi} w_g(d,x',y')Z_{\mathrm{mo}}^{g}(x',y')}{\sum_{(d,x',y')\in\xi} w_g(d,x',y')}, \tag{6}$$

where $\xi=\{(-\pi/4,x-1,y-1),(\pi/4,x-1,y+1),(\pi/4,x+1,y-1),(-\pi/4,x+1,y+1)\}$.

After performing the G value estimation for pixels in Ω_2^g, the zooming process for the G channel of Z_{mo} has been completed. Afterward, the current pattern of Z_{mo} is illustrated in Fig. 17. In Sec. 3.2, the zooming processing for the mosaic R and B channels is presented.

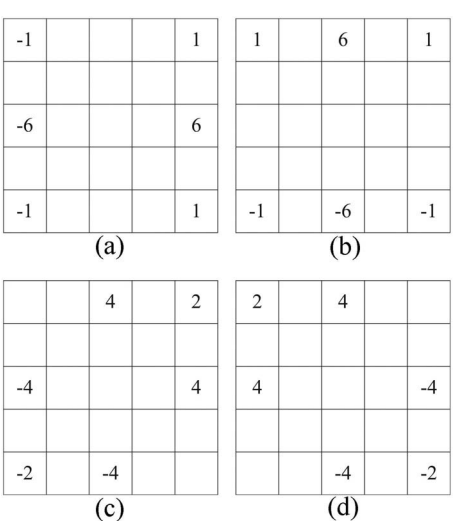

Fig. 16 For all pixels at positions $(x',y') \in \{(x\pm 2m+1, y\pm 2n+1)\}$ in Fig. 12, the four SI-based masks for G channel. (a) The horizontal SI-based mask. (b) The vertical SI-based mask. (c) The $\pi/4$-diagonal SI-based mask. (d) The $-\pi/4$-diagonal SI-based mask.

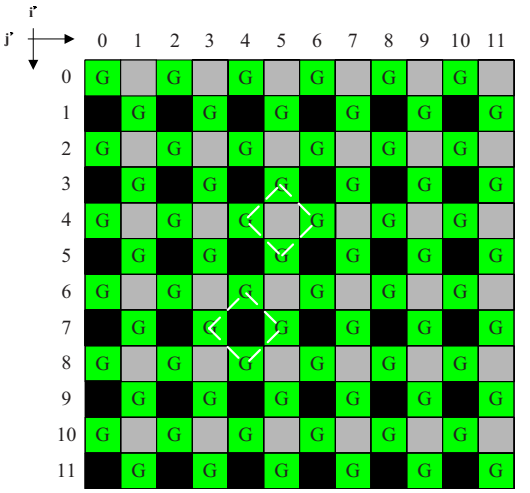

Fig. 17 Current pattern of Z_{mo} after completing the zooming process for the mosaic G channel.

3.2 *Stage 2: Zooming the Mosaic R and B Channels*

In this subsection, the second stage of the proposed zooming algorithm, i.e., the zooming approach for R and B channels, is presented. Since the zooming approach for the mosaic R channel is the same as that for the mosaic B channel, in what follows, we only present it for the mosaic R channel.

For easy exposition, Fig. 18 is taken as the representative to explain how to estimate the R values of pixels in Ω^r. Based on the color difference concept, the R value of the current pixel at position (x,y) can be estimated by

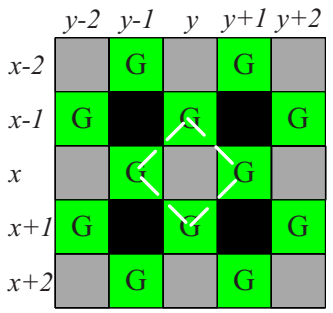

Fig. 18 Subimage used to explain how to estimate the R values of the pixels in Ω^r.

$$Z_{\mathrm{mo}}^{r}(x,y)=\frac{\sum_{(d,x',y')\in\xi} w_g(d,x',y')Z_{\mathrm{mo}}^{g}(x',y')}{\sum_{(d,x',y')\in\xi} w_g(d,x',y')}-D_r(x,y), \quad (7)$$

where $\xi=\{(V,x\pm1,y),(H,x,y\pm1)\}$; the four proper weights are $w_g(V,x-1,y)=1/\{1+[\Sigma_{k=0}^{2}\delta_k\Delta Z_{\mathrm{dm}}^{V,g}(x-k,y)]\}$, $w_g(V,x+1,y)=1/\{1+[\Sigma_{k=0}^{2}\delta_k\Delta Z_{\mathrm{dm}}^{V,g}(x+k,y)]\}$, $w_g(H,x,y-1)=1/\{1+[\Sigma_{k=0}^{2}\delta_k\Delta Z_{\mathrm{dm}}^{H,g}(x,y-k)]\}$, and $w_g(H,x,y+1)=1/\{1+[\Sigma_{k=0}^{2}\delta_k\Delta Z_{\mathrm{dm}}^{H,g}(x,y+k)]\}$, where $\delta_k=2$ if $k=1$; $\delta_k=1$, otherwise.

Finally, the B values of the pixels in Ω^b can be estimated by the same way, and then the fully populated zoomed mosaic image Z_{mo}, as shown in Fig. 19, is obtained.

4 Experimental Results

In this section, based on 24 test mosaic images, some experimental results illustrate the zoomed image quality advantage of our proposed mosaic zooming algorithm when compared with two previous zooming algorithms, one by Battiato *et al.*[33] called the locally adaptive zooming (LAZ) algorithm and the other by Lukac *et al.*[35] called the Bayer pattern zooming (BPZ) algorithm. The three concerned algorithms are implemented on the IBM compatible computer with Intel Core 2 Duo CPU 1.6 GHz and 1 Gbyte RAM. The operating system used is MS-Windows XP and the program developing environment is Borland C++ Builder 6.0. The programs of the three concerned algorithms have been uploaded in Ref. 39.

Figure 20 illustrates the 24 test images from Kodak PhotoCD.[40] Like those test images used in Refs. 33 and 35, in our experiments, the 24 512×728 color test images are first shrunk and down-sampled by Eqs. (8) and (9), respectively, to obtain the 48 256×364 shrunk mosaic images.

$$I_{\mathrm{mo}}(i,j)=\begin{cases} O_{\mathrm{fc}}^{r}(2i,2j) & \text{if } i\in\text{even and } j\in\text{odd} \\ O_{\mathrm{fc}}^{b}(2i,2j) & \text{if } i\in\text{odd and } j\in\text{even} \\ O_{\mathrm{fc}}^{g}(2i,2j) & \text{otherwise} \end{cases}, \quad (8)$$

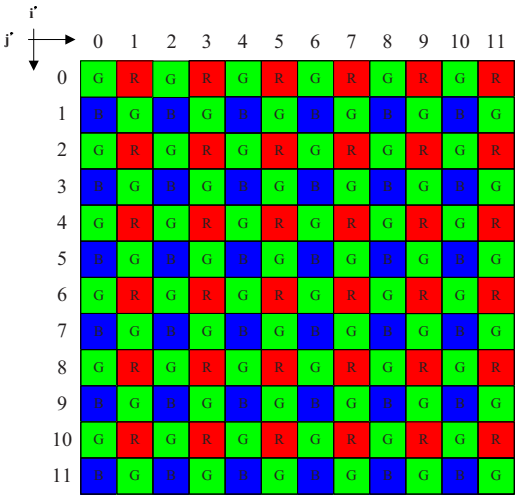

Fig. 19 Fully populated zoomed mosaic image Z_{mo}.

$$I_{\mathrm{mo}}(i,j)=\begin{cases} \frac{1}{4}\sum_{k_1=0}^{1}\sum_{k_2=0}^{1} O_{\mathrm{fc}}^{r}(2i+k_1,2j+k_2) & \text{if } i\in\text{even and } j\in\text{odd} \\ \frac{1}{4}\sum_{k_1=0}^{1}\sum_{k_2=0}^{1} O_{\mathrm{fc}}^{b}(2i+k_1,2j+k_2) & \text{if } i\in\text{odd and } j\in\text{even} \\ \frac{1}{4}\sum_{k_1=0}^{1}\sum_{k_2=0}^{1} O_{\mathrm{fc}}^{g}(2i+k_1,2j+k_2) & \text{otherwise} \end{cases}, \quad (9)$$

where $O_{\mathrm{fc}}^{r}(x,y)$, $O_{\mathrm{fc}}^{g}(x,y)$, and $O_{\mathrm{fc}}^{b}(x,y)$ denote the three color components of the color pixel at position (x,y) in the original full-color image; $I_{\mathrm{mo}}(i,j)$ denotes the color value of the pixel at position (i,j) in the shrunk mosaic image. For convenience, the mosaic images shrunk by Eqs. (8) and (9) are called the shrunk-sampling mosaic image and the shrunk-averaging mosaic image, respectively; the zoomed mosaic images obtained by using the shrunk-sampling mosaic image and the shrunk-averaging mosaic image are called the zoomed-sampling mosaic image and the zoomed-averaging mosaic image, respectively. Furthermore, the boundaries of each image are dealt with using the mirroring method.

We adopt the peak signal-to-noise ratio (PSNR) to justify the advantage of the proposed zooming algorithm. The PSNR of a $M\times N$ mosaic image is defined by

$$\mathrm{PSNE}=10\log_{10}\frac{255^2}{1/(MN)\sum_{i=0}^{M-1}\sum_{j=0}^{N-1}[O_{\mathrm{mo}}(i,j)-Z_{\mathrm{mo}}(i,j)]^2}, \quad (10)$$

where $O_{\mathrm{mo}}(i,j)$ denotes the color value of the pixel at position (i,j) in the 512×728 mosaic image generated by mosaicing the original full-color image and $Z_{\mathrm{mo}}(i,j)$ denotes the color value of the pixel at position (i,j) in the

Fig. 20 Twenty-four test images from Kodak PhotoCD.[40]

zoomed mosaic image obtained by applying the zooming algorithm on I_{mo}.

Table 2 demonstrates the zoomed mosaic image quality comparison in terms of PSNR for the three concerned algorithms. In Table 2, the second to fourth columns and the fifth to seventh columns demonstrate the comparisons for the zoomed-sampling mosaic image and the zoomed-averaging mosaic image, respectively. In Table 2, the entry with the best PSNR is highlighted by boldface. Table 3 demonstrates the average PSNR quality comparison for the zoomed-sampling mosaic image and the zoomed-averaging mosaic image. On average, our proposed zooming algorithm has more than 1.79 dB of quality improvement when compared with two previous zooming algorithms.

Next, we adopt the subjective visual measure to demonstrate the visual quality advantage of our proposed zooming algorithm. For simplicity, seven magnified subimages cut from the test image No. 7 are used to compare the visual effect. Figures 21(a)–21(g) illustrate the seven magnified subimages cut from the mosaic image obtained by mosaicing the original test image No. 7 directly; cut from the zoomed-sampling mosaic images obtained by LAZ algorithm, LAZ algorithm, and the proposed mosaic zooming algorithm; cut from the zoomed-averaging mosaic images obtained by the preceding three concerned algorithms, respectively. To show the mosaic images more clearly, the color value of each pixel is represented by its gray value. Comparing the visual effect between the magnified subimage in Fig. 21(a) and the corresponding one in Figs. 21(b)–21(g), we observe that the shutters in the two zoomed mosaic images obtained by the proposed mosaic zooming algorithm look clearer and have fewer artifacts when compared with those in the other four zoomed mosaic images obtained by the previous zooming algorithms. Similar to the visual comparison for the test image No. 7, we further take the magnified subimages cut from the test image No. 23 for visual comparison. Figures 22(a) and 22(g) illustrate seven magnified subimages cut from the mosaic image obtained by mosaicing original color test image No. 23; cut from the zoomed-sampling mosaic images; cut from the zoomed-averaging mosaic images. From visual comparison, we observe that the face textures of the birds in the two zoomed mosaic images obtained by our proposed mosaic zooming algorithm look clearest and have least artifacts, i.e., the best visual effect.

Besides evaluating the zoomed image quality performance under the mosaic image domain, we further evaluate the image quality performance under the demosaiced full-color image domain. Here, three demosaicing algorithms proposed by Pei and Tam,[22] Lukac and Plataniotis,[21] and Chung and Chan,[4] respectively, are adopted to demosaic the zoomed mosaic images. For convenience, the three demosaicing algorithms proposed in Refs. 22, 21, and 4 are called the signal correlation demosaicing (SCD) algorithm, the normalized color-ratio modeling demosaicing (NCMD) algorithm, and the variance of color differences demosaicing (VCDD) algorithm, respectively.

For fitting the demosaiced full color domain, we adopt three objective color image quality measures, the color PSNR (CPSNR), the S-CIELAB ΔE^*_{ab} metric,[23,41] and the mean structural similarity[42] (MSSIM), and one subjective color image quality measure, the color artifacts, to justify the better quality performance of our proposed zooming algorithm in the demosaiced full color domain. The CPSNR for an $M \times N$ color image is defined by

$$\mathrm{CPSNR} = 10 \log_{10} \frac{255^2}{1/(3MN) \sum_{i=0}^{M-1} \sum_{j=0}^{N-1} \sum_{c \in C} [O^c_{\mathrm{fc}}(i,j) - Z^c_{\mathrm{dm}}(i,j)]^2}, \quad C = \{r,g,b\}, \tag{11}$$

Table 2 PSNR comparison for three concerned algorithms based on mosaic image domain.

	Zoomed-Sampling Mosaic Images			Zoom-Averaging Mosaic Images		
	LAZ (Ref. 33)	BPZ (Ref. 35)	Ours	LAZ (Ref. 33)	BPZ (Ref. 35)	Ours
Image 01	21.0309	22.0561	**24.7832**	21.2226	23.0226	**23.7134**
Image 02	28.2049	28.8876	**31.1006**	28.4293	29.9341	**30.4789**
Image 03	29.0091	29.7613	**32.4967**	29.0248	30.6286	**31.5853**
Image 04	28.0358	28.4953	**31.4473**	27.6440	29.5121	**29.9524**
Image 05	20.9758	21.4357	**25.0237**	20.8922	22.4231	**23.5210**
Image 06	22.9187	23.6897	**26.3666**	23.1881	24.8081	**25.4316**
Image 07	26.3770	27.6181	**31.5838**	25.6686	28.4169	**29.0751**
Image 08	18.7949	19.5576	**22.1909**	18.7016	20.6395	**21.0174**
Image 09	26.2863	27.7866	**30.8980**	25.9515	28.5187	**29.1765**
Image 10	26.9833	27.6467	**30.9190**	26.7956	28.6003	**29.5745**
Image 11	24.3368	24.9773	**27.6679**	24.3862	26.0407	**26.6855**
Image 12	28.2548	29.0543	**31.9817**	28.0030	29.9528	**30.5984**
Image 13	19.4352	19.7921	**22.5522**	19.7506	21.0273	**21.8124**
Image 14	23.7403	24.3755	**26.7303**	23.6557	25.2574	**25.6734**
Image 15	27.6946	28.2269	**30.8834**	27.0980	29.0145	**29.3562**
Image 16	26.5490	27.3799	**29.9867**	26.8854	28.5203	**29.1772**
Image 17	26.8729	27.4734	**30.7729**	26.5713	28.4128	**29.1937**
Image 18	23.0155	23.4576	**26.3295**	23.0911	24.5974	**25.2960**
Image 19	22.5968	23.8859	**26.7228**	22.6393	24.8886	**25.4410**
Image 20	26.2403	27.2153	**30.3149**	25.9125	28.1746	**28.7152**
Image 21	23.1969	24.0252	**27.1012**	23.2785	25.1467	**25.8918**
Image 22	25.6045	26.0330	**28.6118**	25.6056	27.1060	**27.6788**
Image 23	28.3455	29.2668	**32.7028**	28.0118	30.0933	**31.0779**
Image 24	22.0551	22.2335	**25.0977**	22.2721	23.4373	**24.3001**
Average	24.8564	25.5971	**28.5111**	24.7783	26.5906	**27.2677**

where $O^r_{\mathrm{fc}}(i,j)$, $O^g_{\mathrm{fc}}(i,j)$, and $O^b_{\mathrm{fc}}(i,j)$ denote the three color components of the color pixel at position (i,j) in the original full color image; $Z^r_{\mathrm{dm}}(i,j)$, $Z^g_{\mathrm{dm}}(i,j)$, and $Z^b_{\mathrm{dm}}(i,j)$ denote the three color components of the color pixel at position (i,j) in the zoomed and demosaiced full color image. The greater the CPSNR is, the better the image quality is. The S-CIELAB ΔE^*_{ab} of an $M \times N$ color image is defined by

$$\Delta E^*_{ab} = \frac{1}{MN}\sum_{i=0}^{M-1}\sum_{j=0}^{N-1}\left\{\sum_{c\in\Psi}[EO^c_{\mathrm{fc}}(i,j) - EZ^c_{\mathrm{dm}}(i,j)]^2\right\}^{1/2}, \quad \Psi = \{L,a,b\} \tag{12}$$

where $EO^L_{\mathrm{fc}}(i,j)$, $EO^a_{\mathrm{fc}}(i,j)$, and $EO^b_{\mathrm{fc}}(i,j)$ denote the three CIELAB color components of the color pixel at position (i,j) in the original full color image; $EZ^L_{\mathrm{dm}}(i,j)$, $EZ^a_{\mathrm{dm}}(i,j)$,

Table 3 Average PSNR comparison for the zoomed-sampling mosaic image and the zoomed-averaging mosaic image.

	LAZ (Ref. 33)	BPZ (Ref. 35)	Ours
Zoomed-sampling mosaic images	24.8564	25.5971	**28.5111**
Zoomed-averaging mosaic images	24.7783	26.5906	**27.2677**
Average	24.8174	26.0939	**27.8894**
Quality improvement	3.0720	1.7955	

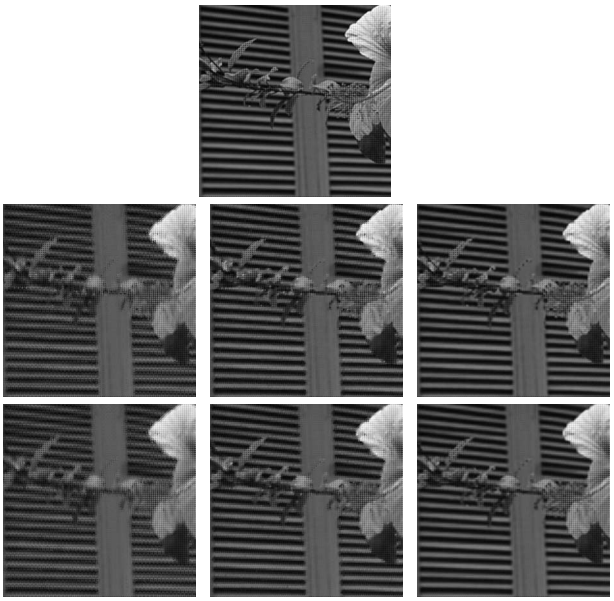

Fig. 21 Seven magnified subimages cut from (a) the mosaic image obtained by mosaicing the original test image No. 7 directly; the ones cut from the zoomed-sampling mosaic images obtained from (b) the LAZ algorithm, (c) the BPZ algorithm, and (d) our proposed mosaic zooming algorithm; the ones cut from the zoomed-averaging mosaic images obtained from (e) the LAZ algorithm, (f) the BPZ algorithm, and (g) our proposed mosaic zooming algorithm.

and $EZ_{\mathrm{dm}}^{b}(i,j)$ denote the three CIELAB color components of the color pixel at position (i,j) in the zoomed and demosaiced full-color image. The smaller the S-CIELAB ΔE_{ab}^{*} is, the better the image quality is. Further, the MSSIM, which is based on human visual system and the comparison between local patterns, is used to measure the image quality performance. The MSSIM for an $M \times N$ color image is defined by

$$\mathrm{MSSIM} = \frac{1}{3}\sum_{c\in\{r,g,b\}}\left(\frac{1}{MN}\sum_{i=0}^{M-1}\sum_{j=0}^{N-1}\frac{\left[2\prod_{\rho\in\Phi}\mu_{\rho}^{c}(i,j)+k_1\right]\left[2\sigma_{oz}^{c}(i,j)+k_2\right]}{\left\{\sum_{\rho\in\Phi}[\mu_{\rho}^{c}(i,j)]^2+k_1\right\}\left\{\sum_{\rho\in\Phi}[\sigma_{\rho}^{c}(i,j)]^2+k_2\right\}}\right),$$

$$\mu_{\rho}^{c}(i,j) = \sum_{x=-5}^{5}\sum_{y=-5}^{5}[w_{xy}I^{c}(i+x,j+y)],$$

$$\sigma_{\rho}^{c}(i,j) = \left(\sum_{x=-5}^{5}\sum_{y=-5}^{5}\{w_{xy}[I^{c}(i+x,j+y)-\mu_{\rho}^{c}(i,j)]^2\}\right)^{1/2}$$

$$\sigma_{oz}^{c}(i,j) = \sum_{x=-5}^{5}\sum_{y=-5}^{5}\left\{w_{xy}\prod_{\rho\in\Phi}[I^{c}(i+x,j+y)-\mu_{\rho}^{c}(i,j)]\right\} \quad (13)$$

where $\Phi\in\{o,z\}$; $I^{c}(i',j')=O_{\mathrm{fc}}^{c}(i',j')$ if $\rho=o$; otherwise, $I^{c}(i',j')=Z_{\mathrm{dm}}^{c}(i',j')$ where the definitions of $O_{\mathrm{fc}}^{c}(i',j')$ and $Z_{\mathrm{dm}}^{c}(i',j')$ are the same as those in Eq. (11); $W=\{w_{x,y}|-5\leq x,y\leq 5\}$ are the coefficients of the 11×11 circular-symmetric Gaussian mask. The greater is the MSSIM, the better is the image quality.

Based on the same test images, among the nine schemes that combine one of the concerned three mosaic zooming algorithms and one of the three existing demosaicing algorithms, Tables 4–6 demonstrate the image quality comparison in terms of the average CPSNR, the average S-CIELAB ΔE_{ab}^{*}, and the average MSSIM, respectively. In Tables 4–6, the second to fourth columns and fifth to seventh columns demonstrate the quality comparison for demosaicing results based on the zoomed-sampling mosaic image and the zoomed-averaging mosaic image, respectively, and the entries with the largest CPSNR and MSSIM, and the smallest S-CIELAB ΔE_{ab}^{*} are highlighted by boldface. From Tables 4–6, we observe that our proposed zooming algorithm produces the best zoomed and demosaiced image quality in terms of CPSNR, S-CIELAB ΔE_{ab}^{*}, and MSSIM.

Finally, we adopt the subjective visual quality measure, color artifacts, to demonstrate the visual quality advantage of our proposed zooming algorithm under the demosaiced full-color domain. After demosaicing the zoomed mosaic image, some color artifacts may appear on nonsmooth regions of the demosaiced image. To evaluate the color artifacts among the concerned algorithms, the magnified subimages containing nonsmooth contents are adopted from the demosaiced images. First, Figs. 23(a)–23(s) illustrate 19 magnified subimages, one cut from the original test image

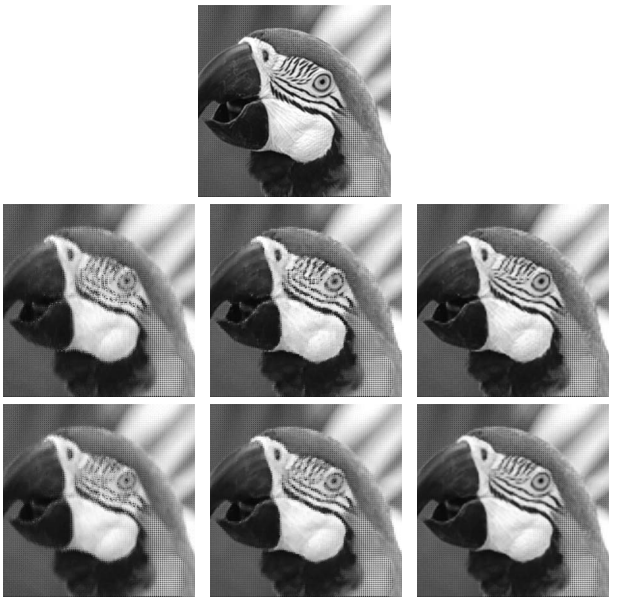

Fig. 22 Seven magnified subimages cut from (a) the mosaic image obtained by mosaicing the original test image No. 23 directly; the ones cut from the zoomed-sampling mosaic images obtained from (b) the LAZ algorithm, (c) the BPZ algorithm, and (d) our proposed mosaic zooming algorithm; the ones cut from the zoomed-averaging mosaic images obtained from (e) the LAZ algorithm, (f) the BPZ algorithm, and (g) our proposed mosaic zooming algorithm.

No. 19; the others cut from the ones by running the nine zooming and demosaicing schemes, which combine one of the three concerned mosaic zooming algorithms and one of the three demosaicing algorithms already mentioned, on the zoomed-sampling mosaic image and the zoomed-averaging mosaic image. From a visual comparison, we observe that based on the same demosaicing algorithm, the demosaiced images, which use the zoomed mosaic images created by our proposed zooming algorithm as the input images, have fewer color artifacts on the plank walls when compared with those that use the zoomed mosaic images created by the other two zooming algorithms as the input images. Further, we take the magnified subimages cut from the test image No. 23 for visual comparison. Figures 24(a)–24(s) are the magnified subimages cut from the original full color test image No. 23 and the 18 zoomed and demosaiced images. Similar to the visual comparison for the test image No. 19, experimental results for the test image No. 23 image also reveal that the face textures of the birds in the demosaiced images, that use the zoomed mosaic images created by our proposed zooming algorithm as the input images, have least color artifacts and the best visual effect. More visual results of the concerned algorithms are available in Ref. 39.

5 Conclusion

The new quality-effective zooming algorithm for mosaic images was presented. Utilizing the adaptive heterogeneity

Table 4 Average CPSNR comparison for three concerned demosaicing algorithms based on demosaiced full-color domain.

	Zoomed-Sampling Mosaic Images			Zoomed-Aveaging Mosaic Images		
	LAZ (Ref. 33)	BPZ (Ref. 35)	Ours	LAZ (Ref. 33)	BPZ (Ref. 35)	Ours
SCD (Ref. 22)	25.2014	25.9048	**28.3469**	24.9344	26.8063	**27.2044**
NCMD (Ref. 21)	25.2456	25.9615	**28.3609**	24.9787	26.8715	**27.2044**
VCDD (Ref. 4)	25.1836	25.8916	**28.3311**	24.9233	26.800	**27.1771**
Average	25.2102	25.9193	**28.3463**	24.9454	26.8259	**27.1916**

Table 5 Average S-CIELAB ΔE^*_{ab} comparison for three concerned demosaicing algorithms based on demosaiced full-color domain.

	Zoomed-Sampling Mosaic Images			Zoomed-Aveaging Mosaic Images		
	LAZ (Ref. 33)	BPZ (Ref. 35)	Ours	LAZ (Ref. 33)	BPZ (Ref. 35)	Ours
SCD (Ref. 22)	4.87254	4.40272	**3.13853**	4.40765	3.87297	**3.28052**
NCMD (Ref. 21)	4.80572	4.22144	**3.08994**	4.34464	3.67143	**3.20609**
VCDD (Ref. 4)	4.82128	4.30877	**3.14600**	4.38060	3.81125	**3.29513**
Average	4.83318	4.31098	**3.12482**	4.37763	3.78522	**3.26058**

Table 6 Average MSSIM comparison for three concerned demosaicing algorithms based on demosaiced full-color domain.

	Zoomed-Sampling Mosaic Images			Zoomed-Aveaging Mosaic Images		
	LAZ (Ref. 33)	BPZ (Ref. 35)	Ours	LAZ (Ref. 33)	BPZ (Ref. 35)	Ours
SCD (Ref. 22)	0.38018	0.47815	**0.60142**	0.32424	0.50118	**0.51600**
NCMD (Ref. 21)	0.38290	0.48475	**0.60543**	0.32682	0.50724	**0.51839**
VCDD (Ref. 4)	0.32424	0.47788	**0.60111**	0.32259	0.50103	**0.51470**
Average	0.36244	0.48026	**0.60265**	0.32455	0.50315	**0.51636**

projection masks and the Sobel-and luminance-estimation-based masks, the gradient information can be extracted from the input mosaic image directly. Then, the extracted gradient information and the color difference concept are combined to assist the design of the proposed quality-effective zooming algorithm. Based on 24 test images, experimental results demonstrated that the proposed zooming algorithm has more than 1.79 dB quality improvement when compared with two previous zooming algorithms, one by Battiato *et al.*[33] and the other by Lukac *et al.*[35] In addition, based on the demosaiced full-color domain, the proposed zooming algorithm has the best image quality

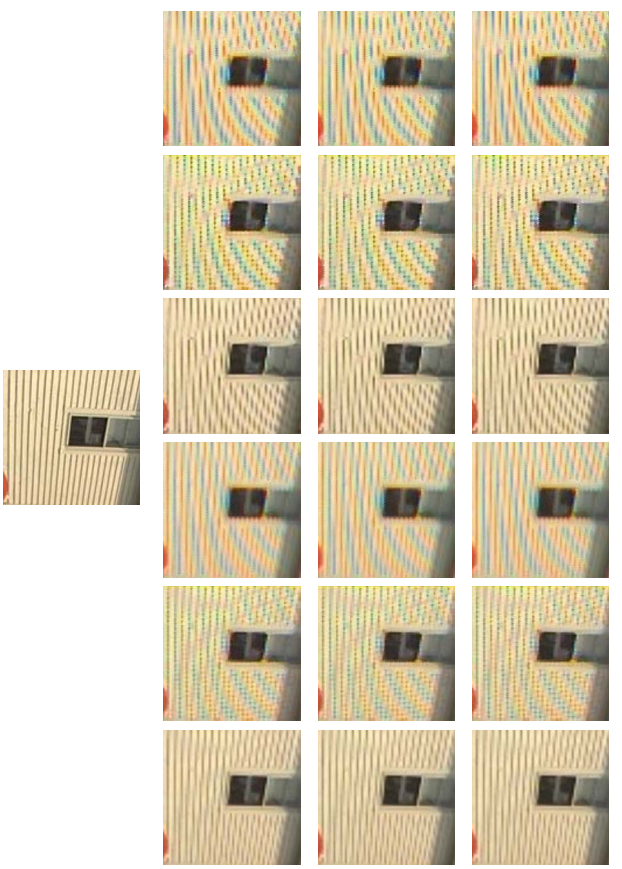

Fig. 23 Nineteen magnified subimages cut from (a) the original test image No. 19; based on the zoomed-sampling mosaic image, the demosaiced full-color images obtained by (b) LAZ+SCD, (c) LAZ+NCMD, (d) LAZ+VCDD (e) BPZ+SCD, (f) BPZ+NCMD, (g) BPZ+VCDD, (h) ours+SCD, (i) ours+NCMD, and (j) ours+VCDD; based on the zoomed-averaging mosaic image, the demosaiced full-color images obtained by (k) LAZ+SCD, (l) LAZ+NCMD, (m) LAZ+VCDD (n) BPZ+SCD, (o) BPZ+NCMD, (p) BPZ+VCDD, (q) ours+SCD, (r) ours+NCMD, and (s) ours+VCDD.

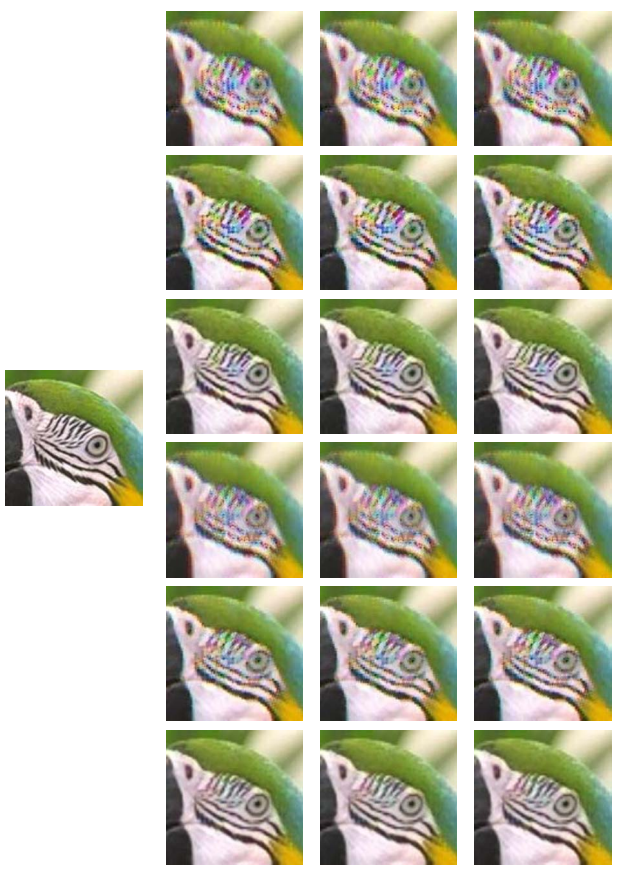

Fig. 24 Nineteen magnified subimages cut from (a) the original test image No. 23; based on the zoomed-sampling mosaic image, the demosaiced full color images obtained by (b) LAZ+SCD, (c) LAZ+NCMD, (d) LAZ+VCDD (e) BPZ+SCD, (f) BPZ+NCMD, (g) BPZ+VCDD, (h) ours+SCD, (i) ours+NCMD, and (j) ours+VCDD; based on the zoomed-averaging mosaic image, the demosaiced full color images obtained by (k) LAZ+SCD, (l) LAZ+NCMD, (m) LAZ+VCDD (n) BPZ+SCD, (o) BPZ+NCMD, (p) BPZ+VCDD, (q) ours+SCD, (r) ours+NCMD, and (s) ours+VCDD.

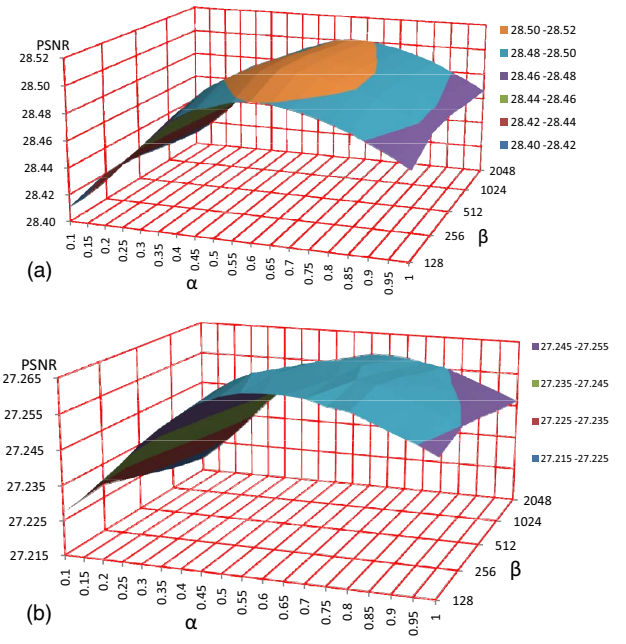

Fig. 25 In terms of α and β, the average CPSNR surfaces for (a) the zoomed-sampling mosaic image and (b) the zoomed-averaging mosaic image.

performance in terms of three measures such as CPSNR, S-CIELAB ΔE^*_{ab}, and MSSIM. For the proposed zooming algorithm, it can only enlarge the original $X \times Y$ mosaic image to the one with a size of $2X \times 2Y$ and it is an interesting research topic to extend the proposed zooming algorithm to enlarge the mosaic image to the one with arbitrary size.

Appendix: The Determination of Two Parameters α and β

Since the zoomed image quality performance of the proposed zooming algorithm is influenced by the two parameters α and β, the determination of the best α and β is discussed in this appendix. In terms of α and β is discussed in this appendix. In terms of α and β, the average CPSNR surfaces of the zoomed-sampling mosaic image and the zoomed-averaging mosaic image are illustrated in Figs. 25(a) and 25(b), respectively. From the peaks of Figs. 25(a) and 25(b), the best choices of α and β are α=0.6 and β =256.

Acknowledgments

This work is supported by the National Science Council of the R.O.C. under Contract Nos. NSC97-2221-E-011-102-MY3 and NSC98-2221-E-011-102-MY3.

References

1. B. E. Bayer, "Color imaging array," U.S. Patent No. 3,971,065 (1976).
2. R. Ramanath, W. E. Snyder, G. L. Bilbro, and W. A. Sander III, "Demosaicking methods for Bayer color arrays," *J. Electron. Imaging* **11**(3), 306–315 (2002).
3. B. K. Gunturk, J. Glotzbach, Y. Altunbasak, R. W. Schafer, and R. M. Mersereau, "Demosaicking: color filter array interpolation," *IEEE Signal Process. Mag.* **22**(1), 44–54 (2005).
4. K. H. Chung and Y. H. Chan, "Color demosaicking using variance of color differences," *IEEE Trans. Image Process.* **15**(10), 2944–2955 (2006).
5. H. J. Trussell and R. E. Hartwig, "Mathematics for demosaicking," *IEEE Trans. Image Process.* **11**(4), 485–492 (2002).
6. X. Li, "Demosaicing by successive approximation," *IEEE Trans. Image Process.* **14**(3), 370–379 (2005).
7. D. D. Muresan and T. W. Parks, "Demosaicing using optimal recovery," *IEEE Trans. Image Process.* **14**(2), 267–278 (2005).
8. D. Alleysson, S. Susstrunk, and J. Herault, "Linear demosaicing inspired by the human visual system," *IEEE Trans. Image Process.* **14**(4), 439–449 (2005).
9. E. Dubois, "Frequency-domain methods for demosaicking of bayer-sampled color images," *IEEE Signal Process. Lett.* **12**(12), 847–850 (2005).
10. D. Menon and G. Calvagno, "Regularization approaches to demosaicking," *IEEE Trans. Image Process.* **19**(10), 2209–449 (2009).
11. B. Gunturk, Y. Altunbasak, and R. Mersereau, "Color plane interpolation using alternating projections," *IEEE Trans. Image Process.* **11**(9), 997–1013 (2002).
12. J. S. J. Li and S. Randhawa, "Color filter array demosaicking using high-order interpolation techniques with a weighted median filter for sharp color edge preservation," *IEEE Trans. Image Process.* **18**(9), 1946–1957 (2009).
13. T. Sakamoto, C. Nakanishi, and T. Hase, "Software pixel interpolation for digital still cameras suitable for a 32-bit MCU," *IEEE Trans. Consum. Electron.* **44**(4), 1342–1352 (1998).
14. D. R. Cok, "Signal processing method and apparatus for producing interpolated chrominance values in a sampled color image signal," U.S. Patent No. 4,642,678 (1987).
15. W. T. Freeman, "Median filter for reconstructing missing color samples," U.S. Patent No. 4,724,395 (1988).
16. H. Hibbard, "Apparatus and method for adaptively interpolating a full color image utilizing luminance gradients," U.S. Patent No. 5,382,976 (1995).
17. J. E. Adams and J. F. Hamilton, "Adaptive color plan interpolation in single sensor color electric camera," U.S. Patent No. 5,506,619 (1996).
18. J. F. Hamilton and J. E. Adams, "Adaptive color plane interpolation in single sensor color electronic camera," U.S. Patent No. 5,629,734 (1997).
19. Y. Hel-Or and D. Keren, "Image demosaicing method utilizing directional smoothing," U.S. Patent No. 6,404,918 (2002).
20. R. Ramanath and W. E. Snyder, "Adaptive demosaicking," *J. Electron. Imaging* **12**(4), 633–642 (2003).
21. R. Lukac and K. N. Plataniotis, "Normalized color-ratio modeling for CFA interpolation," *IEEE Trans. Consum. Electron.* **50**(2), 737–745 (2004).
22. S. C. Pei and I. K. Tam, "Effective color interpolation in CCD color filter arrays using signal correlation," *IEEE Trans. Circuits Syst. Video Technol.* **13**(6), 503–513 (2003).
23. W. Lu and Y. P. Tang, "Color filter array demosaicking: new method and performance measures," *IEEE Trans. Image Process.* **12**(10), 1194–1210 (2003).
24. R. Lukac, K. N. Plataniotis, D. Hatzinakos, and M. Aleksic, "A novel cost effective demosaicing approach," *IEEE Trans. Consum. Electron.* **50**(1), 256–261 (2004).
25. X. Wu and N. Zhang, "Primary-consistent soft-decision color demosaicing for digital cameras (patent pending)," *IEEE Trans. Image Process.* **13**(9), 1263–1274 (2004).
26. L. Zhang and X. Wu, "Color demosaicking via directional linear minimum mean square-error interpolation," *IEEE Trans. Image Process.* **14**(12), 2167–2178 (2005).
27. L. Chang and Y. P. Tan, "Hybrid color filter array demosaicking for effective artifact suppression," *J. Electron. Imaging* **15**(1), 013003 (2006).
28. H. A. Chang and H. H. Chen, "Stochastic color interpolation for digital cameras," *IEEE Trans. Circuits Syst. Video Technol.* **17**(8), 964–973 (2007).
29. K. L. Chung, W. J. Yang, W. M. Yan, and C. C. Wang, "Demosaicing of color filter array captured images using gradient edge detection masks and adaptive heterogeneity-projection," *IEEE Trans. Image Process.* **17**(12), 2356–2367 (2008).
30. R. G. Keys, "Cubic convolution interpolation for digital image processing," *IEEE Trans. Acoust., Speech, Signal Process.* **29**(6), 1153–1160 (1981).
31. S. E. Reichenbach and F. Geng, "Two-dimensional cubic convolution," *IEEE Trans. Image Process.* **12**(8), 857–865 (2003).
32. J. W. Hwang and H. S. Lee, "Adaptive image interpolation based on local gradient features," *IEEE Signal Process. Lett.* **11**(3), 356–362 (2004).
33. S. Battiato, G. Gallo, and F. Stanco, "A locally adaptive zooming algorithm for digital images," *Image Vis. Comput.* **20**(11), 805–812 (2002).
34. R. Lukac and K. N. Plataniotis, "Digital camera zooming on the color filter array," *Electron. Lett.* **39**(25), 1806–1807 (2003).
35. R. Lukac, K. N. Plataniotis, and D. Hatzinakos, "Color image zooming on the Bayer pattern," *IEEE Trans. Circuits Syst. Video Technol.*

15(11), 1475–1492 (2005).
36. R. Lukac and K. N. Plataniotis, "Digital zooming for color filter array," *Real-Time Imag.* **11**(2), 129–138 (2005).
37. R. Gonzalez and R. Woods, *Digital Image Processing*, Addison Wesley, New York (1992).
38. R. Lukac, K. Martin, and K. N. Plataniotis, "Demosaicked image postprocessing using local color ratios," *IEEE Trans. Circuits Syst. Video Technol.* **14**(6), 914–920 (2004).
39. Available online at http://140.118.175.164/WJYang/paper/ZoomCFA/.
40. Available online at http://www.site.uottawa.ca/~edubois/demosaicking/.
41. R. W. G. Hunt, *Measuring Colour*, 2nd ed., Ellis Horwood, Chichester, UK (1995).
42. Z. Wang, A. C. Bovik, H. R. Sheikh, and E. P. Simoncelli, "Image quality assessment: from error visibility to structural similarity," *IEEE Trans. Image Process.* **13**(4), 600–612 (2004).

Kuo-Liang Chung received his BS, MS, and PhD degrees in computer science and information engineering from the National Taiwan University, Taiwan, in 1982, 1984, and 1990, respectively. Prof. Chung was a visiting scholar at the University of Washington, Seattle, in the summer of 1999. He headed the Department of Computer Science and Information Engineering at the National Taiwan University of Science and Technology (NTUST)from 2003 to 2006. He was the executive editor of the *Journal of the Chinese Institute of Engineers* from 1996 to 1998. He received the Distinguished Engineering Professor Award from Chinese Institute of Engineers in 2001, the Distinguished Research Award (2004 to 2007), and Distinguished Scholar Research Project Award (2009–2012) from the National Science Council, Taiwan; the best paper award from the Society of Computer Vision, Graphics, and Image Processing (Taiwan) in 2007. He was an IET fellow in 2009 and became the University Chair Professor at NTUST in 2009. His research interests include image/video compression, image/video processing, algorithms, and multimedia applications.

Wei-Jen Yang received the BS degree in Computer Science and Information Engineering from National Taiwan University of Science and Technology, Taipei, Taiwan, in 2004 and the PhD degree in Computer Science and Information Engineering from National Taiwan University, Taipei, Taiwan, in 2009. He is now a postdoctoral researcher in Department of Computer Science and Information Engineering at National Taiwan University of Science and Technology. His research interests include color image processing, digital camera image processing, image/video compression, computer vision, pattern recognition, and algorithms.

Jun-Hong Yu received his BS degree in mathematics from Fu Jen Catholic University Taipei, Taiwan, in 2007 and he is currently pursuing his PhD degree with the Graduate Institute of Networking and Multimedia at National Taiwan University, Taipei. His research interests include scientific computation, computer vision, numerical linear algebra, image processing, and coding theory.

Wen-Ming Yan received his BS and MS degrees in mathematics from National Taiwan University, Taipei, where he is currently an associate professor of computer science and information engineering. His research interests include scientific computation, image compression, computer vision, numerical linear algebra, image processing, coding theory, and algorithms.

Chiou-Shann Fuh received his BS degree in computer science and information engineering from National Taiwan University, Taipei, in 1983, his MS degree in computer science from the Pennsylvania State University, University Park, in 1987, and his PhD degree in computer science from Harvard University, Cambridge, Massachusetts, in 1992. He was with AT&T Bell Laboratories, Murray Hill, New Jersey, engaged in performance monitoring of switching networks from 1992 to 1993. He was an associate professor with the Department of Computer Science and Information Engineering, National Taiwan University, Taipei, from 1993 to 2000, and then became a full professor. His current research interests include digital image processing, computer vision, pattern recognition, and mathematical morphology.